Tellurium-Doped Iron Borophosphate Glass-Ceramics: Structural, Optical, Antimicrobial, and Anticancer Properties

Vandana A. Gaikwad
Department of Chemistry, Dr. Babasaheb Ambedkar Marathwada University, Sub Campus Osmanabad, Maharashtra India

Radhakrishnan M. Tigote
Department of Chemistry, Dr. Babasaheb Ambedkar Marathwada University, Sub Campus Osmanabad, Maharashtra India
rmtigote.chemobad@bamu.ac.in

Abstract
Glass ceramic nanomaterials as $yTeO_2(100-y)[36Fe_2O_3.10B_2O_3.54P_2O_5]$ (y = 1, 6, 9) were synthesized by the sol-gel method. Their optical, structural, and dielectrical properties were investigated. Results obtained from UV–Visible spectrum predicted that the optical band gap energy decreased from 4.97 to 4.94 eV. X-ray diffraction reveals that BCC structure has a crystalline size from 9.77 to 26.68 nm. The distinct rounded or courous and porous morphological structure of synthesized glass ceramic was examined using FE-SEM. The elemental detection is analyzed with the help of Energy Dispersive X-ray spectroscopy. According to dielectric studies, synthesized glass ceramics shows low dielectric loss as well as dielectric loss tangent (tanδ) decreases at high frequency. Hence it acts as a good conductor. Synthesized glass ceramic material shows good biological activity. Based on the results of antimicrobial and anticancer studies the present glass system may be used in various medical field applications.
Keywords: *Band Width, Morphological Structure, Antimicrobial and Anticancer activity*

1. Introduction

Boro-phosphate glasses have received a lot of attention from researchers due to their greater chemical resistance than the majority of silicate and borosilicate glasses. They have remarkable chemical resistance and a low melting point [1,2]. The heavy metals, phosphates, and sulphates contained in nuclear waste are not very soluble in borosilicate glasses. The next choice for glasses would be phosphate or borophosphate ones. The remarkable chemical resistance of iron phosphate glasses is well recognized. Due to their excellent chemical durability, iron phosphate glasses have proven to be ideal for confirming high-level nuclear waste. As well as ternary alkali borophosphate glasses are far more useful as solid electrolytes than their pure binary alkali borate or phosphate equivalents because of their exceptional physical and chemical stabilities and improved ionic conductivities [3,4]. Iron phosphate glasses have been studied for a range of applications due to their high thermal expansion coefficient, low melting and transition temperatures, optical transmission qualities, and compositional flexibility. Due to their interesting mixture of physical and chemical features, boron-containing iron phosphate glasses have recently attracted a lot of attention. Iron phosphate glasses demonstrated that the addition of boron improved the thermal stability of iron phosphate glasses. Also, it has technological applications like bone transplants [5,6].

The network structure of simple phosphate glass is composed of P tetrahedra that are linked to other neighbouring tetrahedra by bridge oxygens. The addition of boron atoms to the phosphate glass network and the combination of the two network formers, B_2O_3 and P_2O_5, allows for considerable changes to the material properties as opposed to simple borate and phosphate networks alone. A fascinating area of research is the function that P_2O_5 and B_2O_3 play important roles in the glass structure, and they interact with other components of the glass network. Because of this, the merging of borate and phosphate groups that have been doped with 3d transition metal ions is an interesting topic in the field of glass research [7]. Borate glasses are electrically semiconducting when iron is added to them. The quantitative characteristics of modifiers determine the amount of iron present in the glass in various valence states, which can be in +2 or +3 depending on the oxygen atoms that are accessible [8-10]. Fe^{3+} ions are present in both tetrahedral and octahedral configurations, whereas Fe^{2+} ions are restricted to sixfold coordination within glass structures, contributing to their modifying role. A high concentration of P_2O_5 and B_2O_3 modifiers can enhance bioactivity, making them appealing for biomedical glass fibers. However, these glasses tend to crystallize at the temperatures typically required for fiber drawing. In biomedical applications such as bone regeneration and reconstruction, phosphate glasses serve as favourable alternatives to silicate glasses [11-13]. It has been investigated that by adding B_2O_3 to iron borophosphate glass ceramics, it increases the thermal stability while having little impact on its chemical resistance. The results suggest that iron

borophosphate glass ceramics possess optical properties [14]. The majority of the research on iron phosphate glasses has been on simple binary, ternary, or quaternary glasses made of P_2O_5, Fe_2O_3, and a few other elements [15]. Fe_2O_3 has been discovered to be an efficient oxide for bioactivity in various glasses, among other transition metal oxides. Infact, it has already been established that bioactive glasses can create apatite increases as their Fe_2O_3 content rises. Also, it was established that Fe^{3+} ions play a critical role in boosting bone metabolism when combined in the right proportions with bioactive glasses [16]. Fe_2O_3 is interesting due to a wide range of physical and chemical characteristics as well as its antibacterial effects. The interesting concept for the predictable future is to improve bioglass antibacterial characteristics and make it useful for various medicinal purposes. The rich structural chemistry of borophosphate glasses and their use in heterogeneous catalysis, photonics, ion exchange, and other areas give them importance [17,18]. It may be advantageous to increase the chemical stability of phosphate-based glasses by having the ability to dissolve certain metal oxides (MO). As a result of depolymerising P-O-P structures and replacing weak $P\text{-}O^-M^+$ connections with stronger P-O-M bonds, the inserting of metallic ions (Mn^+) enhances chemical resistance [19]. Additionally, bioactive borate glasses are now generating more interest. The variety of dopant elements, such as Sr, Cu, Zn, Ag, and V, which may be found in the human body and are known for having positive impacts on bone metabolism, have been researched for their behaviour. An are form borate, and phosphate bioactive glasses are some of these materials [20]. Although P_2O_5 and B_2O_3 are water-soluble glass-forming oxides, their combination with modifier oxides results in the development of borophosphate glass that is significantly more chemically resistant because B-O-P bridges between phosphate (PO_4) and borate (BO_4, BO_3) structural units. As a result of the addition of glassy TeO_2, it is made up of TeO_4 structural units (as opposed to TeO_{3+1}), in which three Te-O bonds are shorter and one longer. Li_2O and other modifier oxides increase the tendency of TeO_2 to form glasses and the capacity of TeO_4 to convert into triangular, pyramidal structural units in TeO_3. According to present research, the structure and properties of borophosphate glasses modify as TeO_2 concentration increases. The doping of tellurium oxide on phosphate and borophosphate glasses often increases transparency in the ultraviolet and infrared spectrums as well as the refractive index, making these glasses potentially glamorous materials for the production of various optical and optoelectronic devices. TeO_2 is also known to improve the chemical resistance and thermal stability of borophosphate glasses, which is a common problem associated with the drawing of glass fibres [21]. The significant glass type known as borophosphate glass has a number of beneficial qualities. Because it has a low melting point, superior chemical resistance, and high irradiation stability, borophosphate glass containing iron is also one of the most promising matrices [22]. The development of glass ceramics allows for the modification of ceramics chemical, mechanical, and electrical properties [23,24].

Impedance spectroscopy analysis of iron phosphate glasses revealed improved electrical properties, but no clear connection was found between electronic and ionic conduction variation [25]. It has been demonstrated that doping iron phosphate glasses with boric oxide increases their chemical, thermal, and crystallisation resistance, as well as their resistance to strong radiation. TeO_2 is a conditional glassmaker that can create glass when combined with network modifiers including Li_2O, AgO, MgO, ZnO, and rare earth oxides. The conductivity and stability of the borate-glass network are improved by the addition of TeO_2 at lower mole percentages [26,27].

However, due to the quality of the structure, diseases like bone abnormalities have become widespread, increasing the therapeutic demands on tissue regeneration and wound healing. Therefore, one important area that academics are investigating and attempting to highlight is the advancement of new manufacturing methods for borophosphate. For borophosphate glass material, standard solid-state sintering, melt quenching, and subsequent crystallisation have proven to be the most widely utilised preparation processes. The disadvantage of solid-state sintering and melting techniques is the evaporation of the volatile component when processing at high temperatures. In contrast, the sol-gel approach offers great chemical uniformity while requiring low processing temperatures. With the use of this technique, a wide range of compositions can be produced in several different shapes, including powders, coatings, and fibers. Additionally, bioceramics produced using the sol-gel process exhibit porosity and larger

surface areas, both of which are advantageous for the bioactivity with low-cost raw materials for sol-gel processing of bioceramics.

The sol-gel technology was used to design the glass ceramic in order to more effectively dissolve the greatest amount of doping in it. Additionally, to achieve good homogeneity and little phase separation, a chemical bottom-up sol-gel method is helpful. Therefore, a sol-gel technique was employed to produce our present work, $yTeO_2(100\text{-}y)[36Fe_2O_3.10B_2O_3.54P_2O_5]$ Where y = 1,6,9 borophosphate using tellurium and iron oxide with the objective of providing a method for producing cost-effective applications in the biomedical field [28,29]. As a result, the sol-gel process has essentially come to be associated with nanomaterials, particularly in the context of glasses that briefly discuss their potential for biomedical uses like bone maintenance, immunological function, and osteogenic effects, which allow for cell attachment (osteoblasts) and subsequent growth [30]. Making bioactive glasses more flexible in regard to doping with particular metals, such as iron, which stimulates their biological performance, is a benefit of partially or completely replacing SiO_2 with P_2O_5 and B_2O_3. Due to its less antibacterial capabilities, iron has a long history of being well-known. Doping bioactive glasses with iron may encourage the breakdown of microorganism resistance, acting against bacterial activity [31]. And tellurium has been incorporated into bioactive glasses, such as silica-based glasses, to enhance their biological properties. The addition of tellurium dioxide (TeO_2) in small amounts does not disrupt the glass's amorphous nature but can alter its thermal properties and promote the formation of hydroxyapatite, a key component for bone regeneration [32].

These properties are particularly valuable in addressing pressing healthcare challenges such as antimicrobial resistance and cancer, which are significant global health concerns. Tellurium nanoparticles have demonstrated cytotoxic effects against various cancer cell lines, including breast cancer and melanoma cells. These effects are observed at relatively low concentrations, indicating the potential of TeNPs as anticancer agents. Importantly, these nanoparticles show minimal cytotoxicity towards normal cells, suggesting a degree of selectivity in targeting cancerous cells [33]. The development of such materials is part of a broader trend towards utilising bioactive glasses, which are known for their ability to release therapeutic ions, thereby enhancing biological responses while maintaining the structural integrity and amorphous nature of the glass [34]. Tellurium nanostructures synthesised using green nanotechnology approaches have shown significant antibacterial activity against resistant strains such as Methicillin-resistant *Staphylococcus aureus* and multidrug-resistant *Escherichia coli*. While other dopants like copper and zinc also exhibit antimicrobial properties, tellurium is particularly noted for not adversely affecting cell viability or immune response, unlike silver, which significantly decreases cell viability [35]. Although the primary focus has been on antibacterial effects, some research indicates that tellurium nanoparticles may also possess antifungal properties, although higher concentrations may be required compared to antibacterial applications [36].

In this work, we prepared $yTeO_2(100\text{-}y)[36Fe_2O_3.10B_2O_3.54P_2O_5]$ glass material by sol-gel method. Investigating the structural, electrical, morphological, and microbiological characteristics of $yTeO_2(100\text{-}y)[36Fe_2O_3.10B_2O_3.54P_2O_5]$ glasses throughout a range of TeO_2 concentrations is the goal of this study. TGA was used to study the thermal properties. The optical band gap and absorption peak are intended to be measured using UV-visible spectroscopy. Utilising X-ray diffraction, the structural characteristics of the glasses were determined. Scanning electron microscopy (FE-SEM) is used to examine molecule shape. Using EDS, the elemental percentage composition analysis was done. The dielectric loss tangent (tan δ) and dielectric loss were calculated using the dielectric constant. We employed a traditional zone of inhibition test to assess the antibacterial properties of two or three representative specimens in some bacterial cultures in order to further study the multifunctionality of the current samples.

1.2 Experimental Work

1.2.1 Chemicals

The analytical-grade AR chemicals such as iron nitrate $Fe(NO_3)_3.9H_2O$, boric acid (H_3BO_3), ammonium di-hydrogen Orthophosphate ($H_9N_2PO_4$), and telluric acid $Te(OH)_6$ were used as Fe, B, P, and Te sources for the synthesis of $yTeO_2(100\text{-}y)[36Fe_2O_3.10B_2O_3.54P_2O_5]$.

1.2.2 Synthesis of glass ceramics $yTeO_2(100-y)[36Fe_2O_3.10B_2O_3.54P_2O_5]$

For the synthesis of glass ceramics $yTeO_2(100-y)[36Fe_2O_3.10B_2O_3.54P_2O_5]$ (y = 1, 6, 9), the used precursors are telluric acid $Te(OH)_6$, boric acid (H_3BO_3), ammonium di-hydrogen orthophosphate ($H_9N_2PO_4$), and iron nitrate $Fe(NO_3)_6$. All these precursors were added with 20 ml of distillate water in a beaker. The reaction mixture was stirred for 2 hours with an acidic pH. After that, the reaction mixture was heated at 80-90^oC to form a gel within 2 hours. At the same temperature, within 2 hours the gel was fully dried to produce a fine powder of $yTeO_2(100-y)[36Fe_2O_3.10B_2O_3.54P_2O_5]$. This raw glass ceramic powder was calcined at 600^oC for eight hours and used suitable for all subsequent characterisations.

1.2.3 Experimental method for antimicrobial activity

Dimethyl sulfoxide (DMSO) was used to dissolve the glass components, resulting in a final concentration of 10 mg/mL. For the evaluation of bacterial and fungal activity, respectively, standard antimicrobial agents gentamicin and clotrimazole were utilised. First, pathogenic cultures were added to nutritional broth, and they were then incubated for 24 hours at 37°C. Using sterile saline, the broth's turbidity was carefully controlled to reach a standardised value of 0.5 McFarland. A 200 µl diluted suspension of the pathogen was evenly distributed across Muller-Hinton agar plates. Wells were created on the agar plates, and 100 µl of each compound was separately added to them. Additionally, another well was filled with 100 µl of DMSO without the compound to evaluate its effect on bacterial growth. The plates were incubated at 37 °C for 24 hours, and the inhibition zones were carefully examined during this period. The absence of growth around the well was considered a positive result. The inhibitory zone's diameter was measured in millimeters (mm). The minimum inhibitory concentration was determined using the glass compounds $yTeO_2(100-y)[36Fe_2O_3.10B_2O_3.54P_2O_5]$ (y = 1, 6, 9), selected based on their largest inhibition zones. All experiments were performed in triplicate, and the results were expressed as mean values.

1.2.4 Experimental process for anticancer activity

Compounds demonstrating superior antimicrobial efficiency were selected for further assessment of their anticancer properties. Anticancer activity was evaluated against human breast cancer cell line MCF-7, human cervical cancer cell line HeLa, and human ovarian cancer cell line SK-OV-3 using the sulforhodamine B (SRB) assay method. The cancer cell lines were first cultured in a medium supplemented with 10% fetal bovine serum and 2 mM L-glutamine. The experiments were conducted using 96-well microtiter plates. One hundred microliters of the sample were added to each well, which contained 5000 cells per well. The plates were then incubated under controlled conditions at 37°C, with 5% CO_2, 95% air, and 100% relative humidity for 2 hours. Prior to administering the investigational drug, the compound was diluted in an appropriate solvent to reach a concentration of 100 mg/ml. This solution was then further diluted with distilled water to obtain a final concentration of 1 mg/ml and stored frozen until needed. When the drug was applied, an aliquot of the frozen concentrate at 1 mg/ml was thawed and then diluted to concentrations of 100 µg/ml, 200 µg/ml, 400 µg/ml, and 800 µg/ml in a complete medium containing the test article. Aliquots of 10 µl from these dilutions were added to wells containing 90 µl of the medium, resulting in the final drug concentrations of 10 µg/ml, 20 µg/ml, 40 µg/ml, and 80 µg/ml. The plates were incubated under standard conditions for 48 hours, after which cold trichloroacetic acid was added to halt the assay. Cellular fixation to the microtiter plate was accomplished by adding 30% TCA to achieve a final concentration of 10%, followed by incubation at 4 °C for 1 hour. The supernatant was then removed, and the plates were washed five times with tap water before being left to air-dry. Fifty microliters of sulforhodamine B (SRB) at a concentration of 0.4% (w/v) in 1% acetic acid were added to each well, and the plates were incubated at room temperature for 20 minutes. After staining with SRB, the unbound dye was removed, and any remaining dye was eliminated by washing the plates five times with 1% acetic acid. The plates were air-dried, and the dye that had adhered to the cells was recovered using a 10-mM Trizma base solution. The absorbance of the microtiter plates was measured at wavelengths of 540 nm and 690 nm. The percentage growth of cancer cells was calculated by comparing the test wells with the control wells using a standard formula, with calculations performed for each plate, comparing the test wells to the control wells. This

growth measurement was expressed as the ratio of the average absorbance of the test wells to the average absorbance of the control wells, multiplied by 100.

$$\text{Percentage Growth} = \frac{\text{Average absorbance of the test well}}{\text{Average absorbance of the control well}} \text{ x } 100$$

1.3 Result and Discussion

The glass ceramic $yTeO_2(100\text{-}y)[36Fe_2O_3.10B_2O_3.54P_2O_5]$ (y = 1, 6, 9) has been successfully synthesised using the sol-gel technique. The thermal properties were examined by using TGA. An ultraviolet-visible spectrophotometer is used to determine a maximum absorption peak and band gap. XRD was used to determine the interplanar distance, lattice parameter, X-ray density, crystal structure, and particle size. The field emission scanning electron microscopy (FE-SEM) was used to analyse the structural morphology. EDS provides fundamental sequence analysis. The dielectric constant was used to calculate the loss tangent and dielectric loss. Using MIC testing, it was possible to identify the synthetic glass material that exhibited antimicrobial activity.

1.3.1 Thermal Analysis

The current study shows that the thermal expansion coefficient value decreases as the amount of Fe_2O_3 increases [8]. **Figure 1.1** demonstrates the simultaneous thermogravimetric analysis of the crude powder sample. The thermogravimetric measurement curve showed three distinctive stages of mass reduction. The initial stage was observed in the temperature region of 30°C-200°C with a mass reduction of about 0.75%, and it appeared to stage-I correspond to the elimination of adsorbed water. The next stage of mass reduction, which was accomplished in the temperature region of 200°C-400°C, exhibited a small mass reduction of 0.53%, which was related to chemically adsorbed water dehydration [21]. The final stage of mass reduction is shown at a temperature range of 400°C-700°C, exhibiting mass loss of 2.93%. This could be recognised as the elimination of by-products from incomplete condensation of the starting materials, mostly due to the elimination of nitrate ions [22]. Thermogravimetry is the most reliable analysis used to determine the calcination temperature of dried samples derived from the sol-gel technique. The temperature at 600°C which the mass reduction becomes constant. Hence, the synthesised glass ceramic material shows 95.79% thermal stability [23].

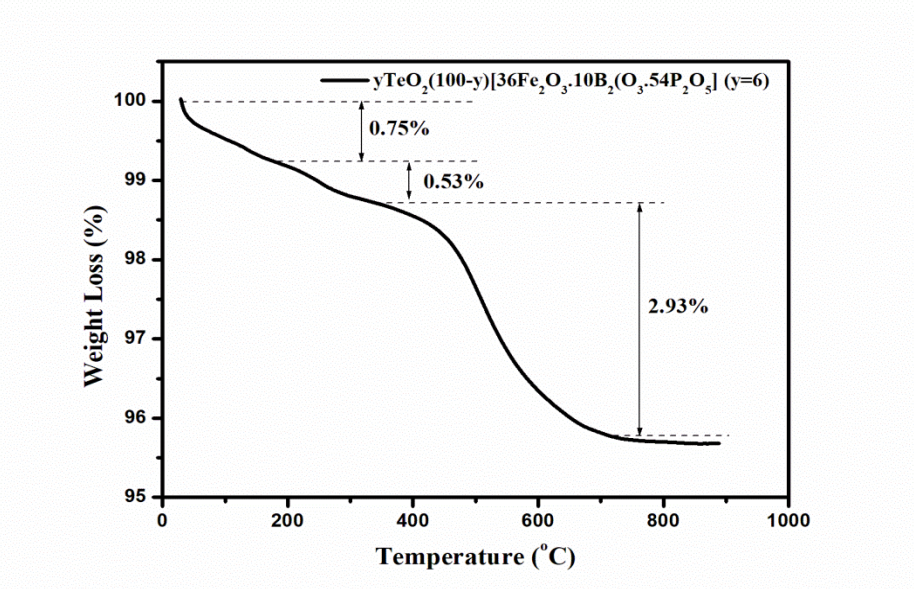


Figure 1.1 TGA plot of $Al_xTeO_3YB_2O_3[(6\text{-}x\text{-}Y)P_2O_5]$

1.3.2 Optical Study

For the analysis of the optical properties of a $yTeO_2(100\text{-}y)[36Fe_2O_3.10B_2O_3.54P_2O_5]$ (y = 1, 6, 9) glass ceramic material, the UV-visible spectrophotometer is used. In the experimental result, all samples were soluble in a 0.01M HNO_3 solution for analysing the maximum absorption peak in the 200–800 nm range. The broad and intense band observed at 302.07 nm is depicted in **Figure 1.2(a)**. The band gap of all samples were calculated using the indirect TAUC plot,

which was 4.97, 4.95, and 4.94 eV, respectively is shown in **table 1**. As determined using Tauc's plot relationship, the optical band gap is stated as follows:

$$(\alpha h\upsilon)^{1/n} = C\,(h\upsilon - Eg) \qquad \text{---------- (1)}$$

Where α = the absorption coefficient, ν = frequency (ν = c/λ, h is Planck's constant, λ = wavelength, c = speed of light), n = 1/2 for indirect optical band gap, respectively, C = proportionality constant, and Eg = band gap. The confirming band gap decreases as the concentration of iron decreases with increases in the concentration of tellurium [7]. The band gap spectrum is shown in **Figure 1.2(b)** With a progressive increase in TeO_2 concentration, the optical band intensity steadily decreases.

Table 1: Optical band gap of $yTeO_2(100-y)[36Fe_2O_3.10B_2O_3.54P_2O_5]$

Sr. No.	% Doping of y	Optical Band Gap (eV)
1	1	4.97
2	6	4.95
3	9	4.94

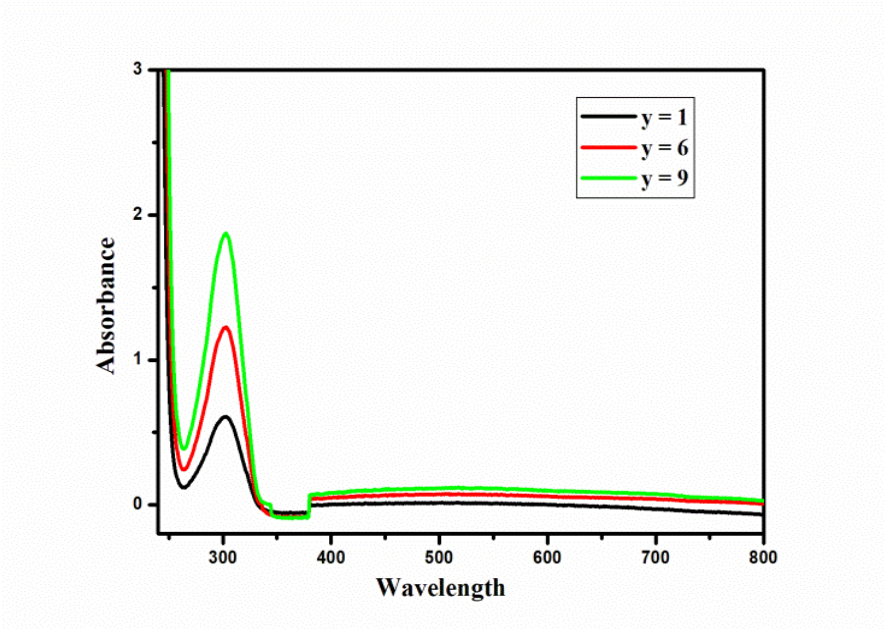


Figure 1.2 a) UV - Visible spectra of $yTeO_2(100-y)[36Fe_2O_3.10B_2O_3.54P_2O_5]$

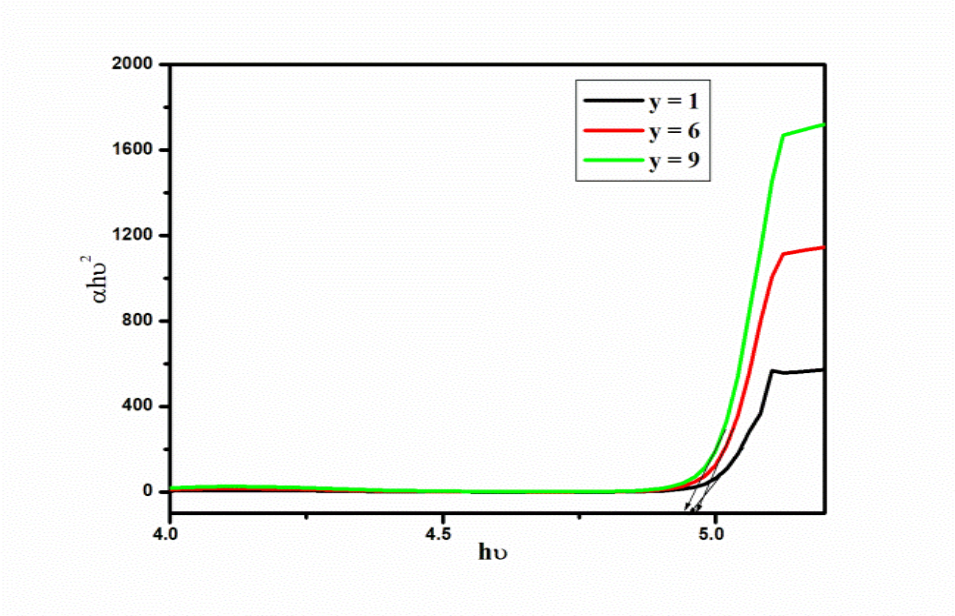


Figure 1.2 b) TAUC Plot of $yTeO_2[100-y)(36Fe_2O_3.10B_2O_3.54P_2O_5]$

1.3.3 Structural study

Figure 4.3 shows the XRD pattern of the three samples with different Te doping concentrations of glass ceramic material having a series of $TeO_2(100\text{-}y)[36Fe_2O_3.10B_2O_3.54P_2O_5]$ (y = 1, 6, 9). All the diffraction peaks are sharp, diffraction peaks as the tellurium concentration is raised, indicating the presence of a crystalline phase in the glass ceramic material [9,10]. The peaks indicate planes (200), (200), (210), (211), (311), and (420), which shows the BCC structure having a particle size ranging from 9.77 to 26.68 nm, which is calculated by using the Debye-Scherer equation as,

$$D = \frac{0.9\lambda}{\beta\cos\theta} \qquad \text{----------(2)}$$

Where λ = 1.543A°,β = Full width of half maxima. The interplanar distance d was calculated by using the formula

$$d = \lambda/2\sin\theta \qquad \text{---------- (3)}$$

The lattice parameter a is given as,

$$a = d\sqrt{h^2 + k^2 + l^2} = \qquad \text{---------- (4)}$$

The volume is given by,

$$V = a^3 \qquad \text{----------(5)}$$

As the concentration of Tellurium increases, the interplanar distance (d) as well as X-ray density increase, respectively. But the lattice constant (a) and volume (V) goes on decreasing. According to **Table2**, as the X-ray density rises, the average particle size (D) similarly rises with an increase in TeO_2 concentration [11].

Figure 1.4 shows a decreasing concentration of octahedral and tetrahedral sites, according to dat a from **Table 3**. The variation in the lattice constant is shown in **Figure 1.5**. **Figure 1.6** depicts the variance in crystalline size. The opposed relationship between unit cell volume and x-ray density is seen in **Figure 1.7**.

Table 2 Inter planar distance (d), Lattice constant (a), Volume (V), X-ray density (d_x), Particle size(D), and Crystal Structure of $yTeO_2(100\text{-}y)[36Fe_2O_3.10B_2O_3.54P_2O_5]$

Sr. No	y	d	a	V	d_x X 10^{-23}	D(nm)	Crystal Structure
1.	1	2.5366	6.9620	337.44	54998.81	9.77	BCC
2.	6	2.6439	6.8097	315.82	55830.37	24.28	BCC
3.	9	2.6028	6.6940	299.95	56929.87	26.68	BCC

Table 3 Hopping lengths 'L_A' & 'L_B' of $yTeO_2(100\text{-}y)[36Fe_2O_3.10B_2O_3.54P_2O_5]$ series

Sr. No.	y	L_A	L_B
1.	1	3.015	4.923
2.	6	2.948	4.815
3.	9	2.899	4.733

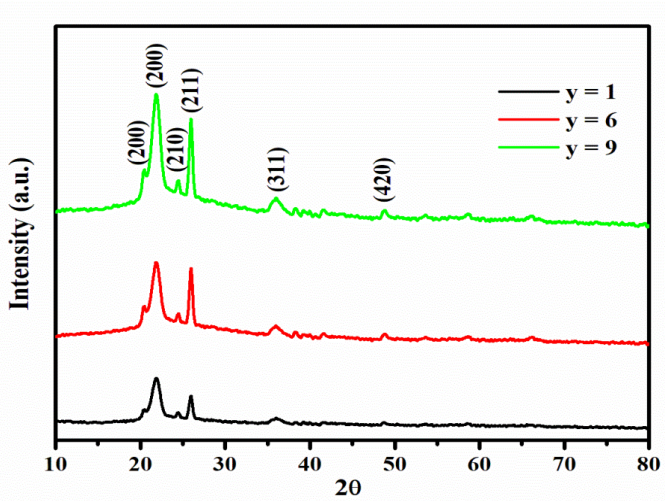


Figure 1.3 XRD spectra of $yTeO_2(100\text{-}y)[36Fe_2O_3.10B_2O_3.54P_2O_5]$ series

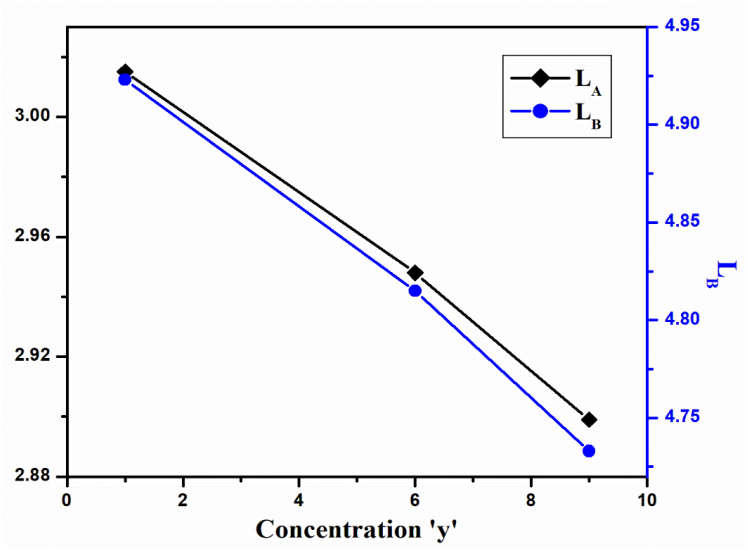


Figure 1.4 Hooping length of $yTeO_2(100-y)[36Fe_2O_3.10B_2O_3.54P_2O_5]$ series

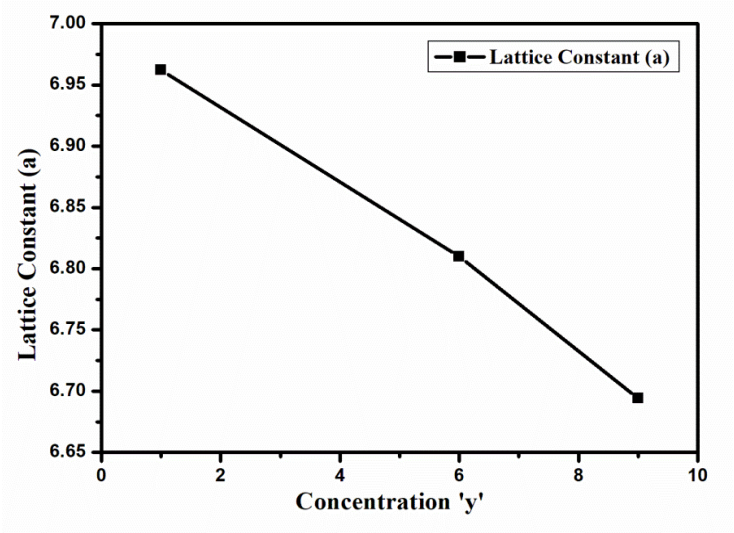


Figure 1.5 Variation of Lattice constant with Concentration of 'y' for $yTeO_2(100-y)[36Fe_2O_3.10B_2O_3.54P_2O_5]$ series

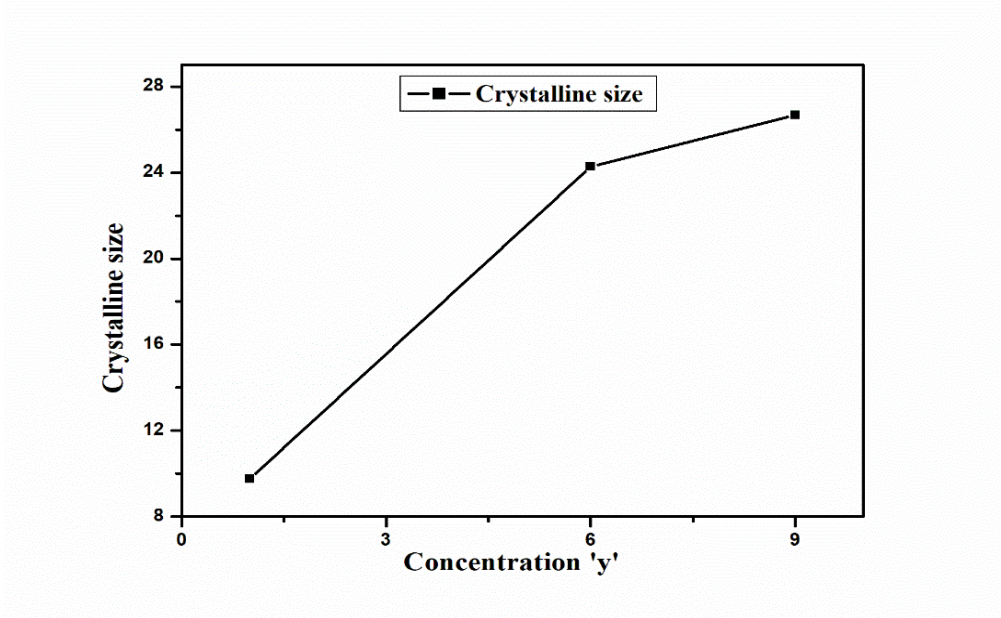


Figure 1.6 Variation of Crystalline size with Concentration 'y' for $yTeO_2(100-y)[36Fe_2O_3.10B_2O_3.54P_2O_5]$ series

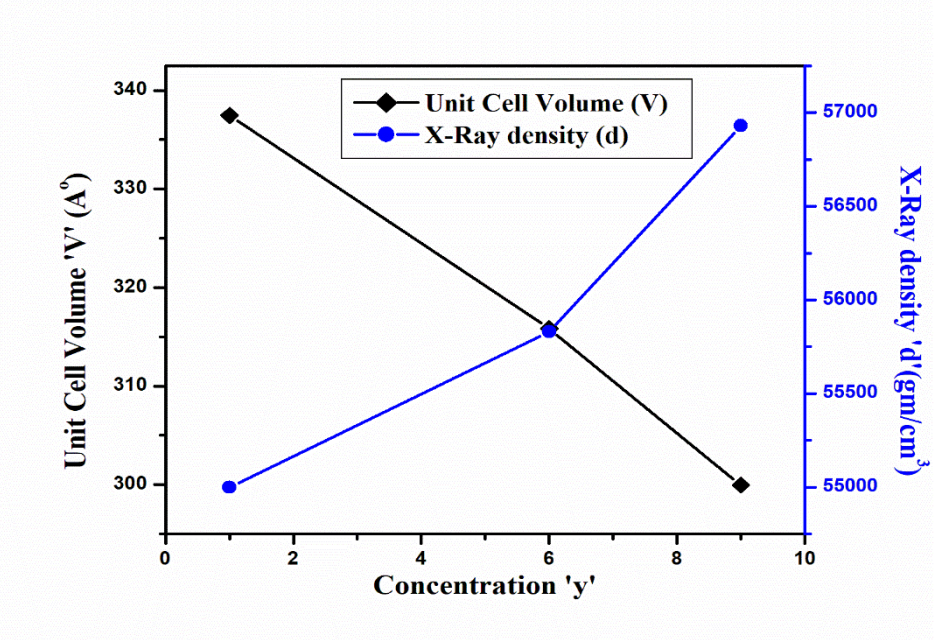
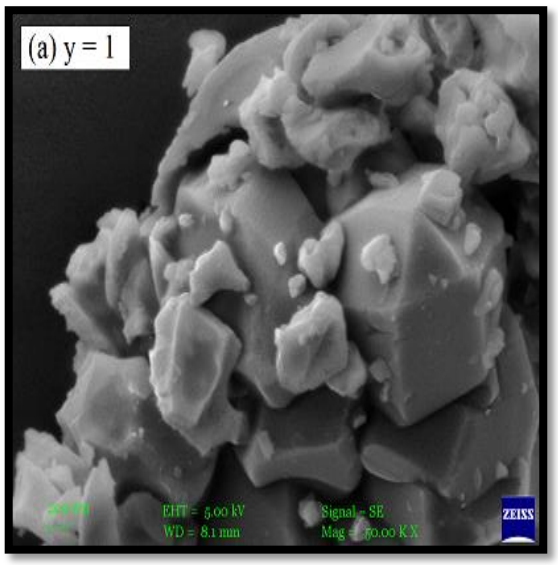
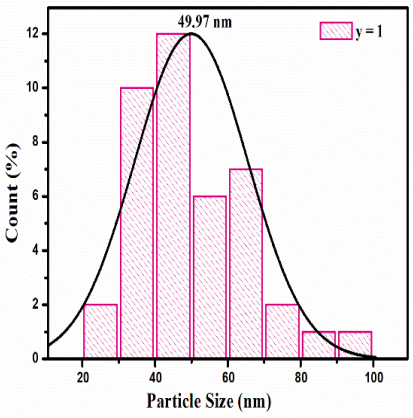


Figure 1.7 Variation of unit cell volume and X-ray density with Concentration 'y' for $yTeO_2(100-y)[36Fe_2O_3.10B_2O_3.54P_2O_5]$

1.3.4 Field Emission Scanning Electronic Microscopy (FE – SEM)

The structural and morphological shape of $yTeO_2(100-y)[36Fe_2O_3.10B_2O_3.54P_2O_5]$ glass ceramic material at different concentrations where (y = 1, 6, 9) have been seen in the images of **Figures (1.8 a, b, and c)**. All three images shows a flower type of morphological structure with a pure glassy surface. With an increase in TeO_2 content, the flower type crystal phase increases [20]. According to histogram the size of the material is 49.97nm, 52.53nm, and 71.24nm for their respective atomic weight %.





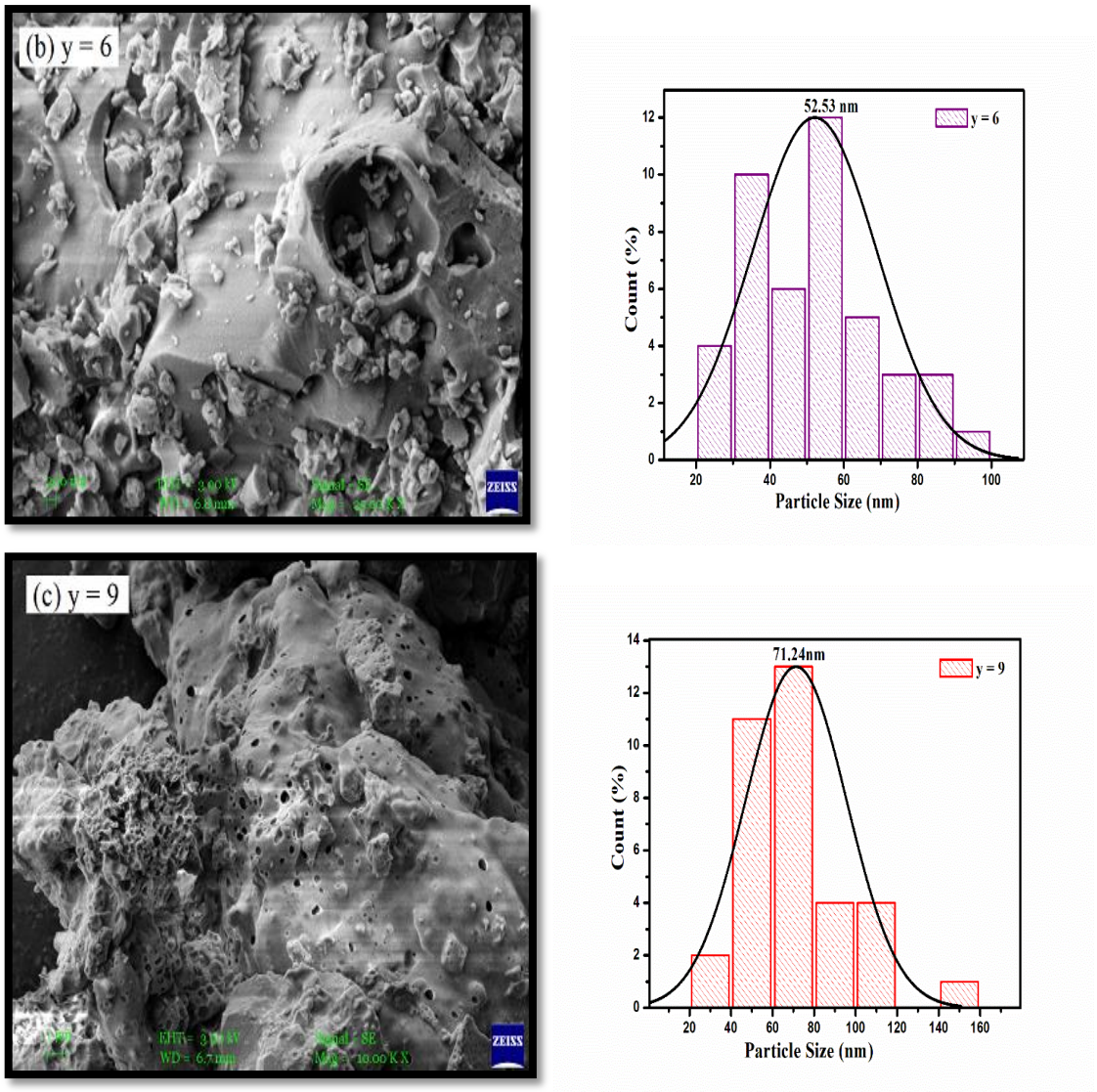


Figure 1.8 FE – SEM Micrograph of $yTeO_2(100-y)[36Fe_2O_3.10B_2O_3.54P_2O_5]$series

1.3.5 Energy Dispersive X-Ray Spectroscopy (EDS)

The elemental composition of $yTeO_2(100-y)[36Fe_2O_3.10B_2O_3.54P_2O_5]$ is analysed using energy-dispersive X-ray analysis. This spectroscopy was performed on annealed samples to establish the presence of the Te, Fe, B, O, and P elements illustrated in **Figure 1.9 (a, b, and c).** The distribution of elements in the samples structural phase is shown in **Figure 1.9 (a-c)**.

According to the elemental detection, there are no impurities in the synthesised glass substance. The elemental mass composition in weight percentage and atomic percentages are co-related and given in **Tables 4 and 5.**

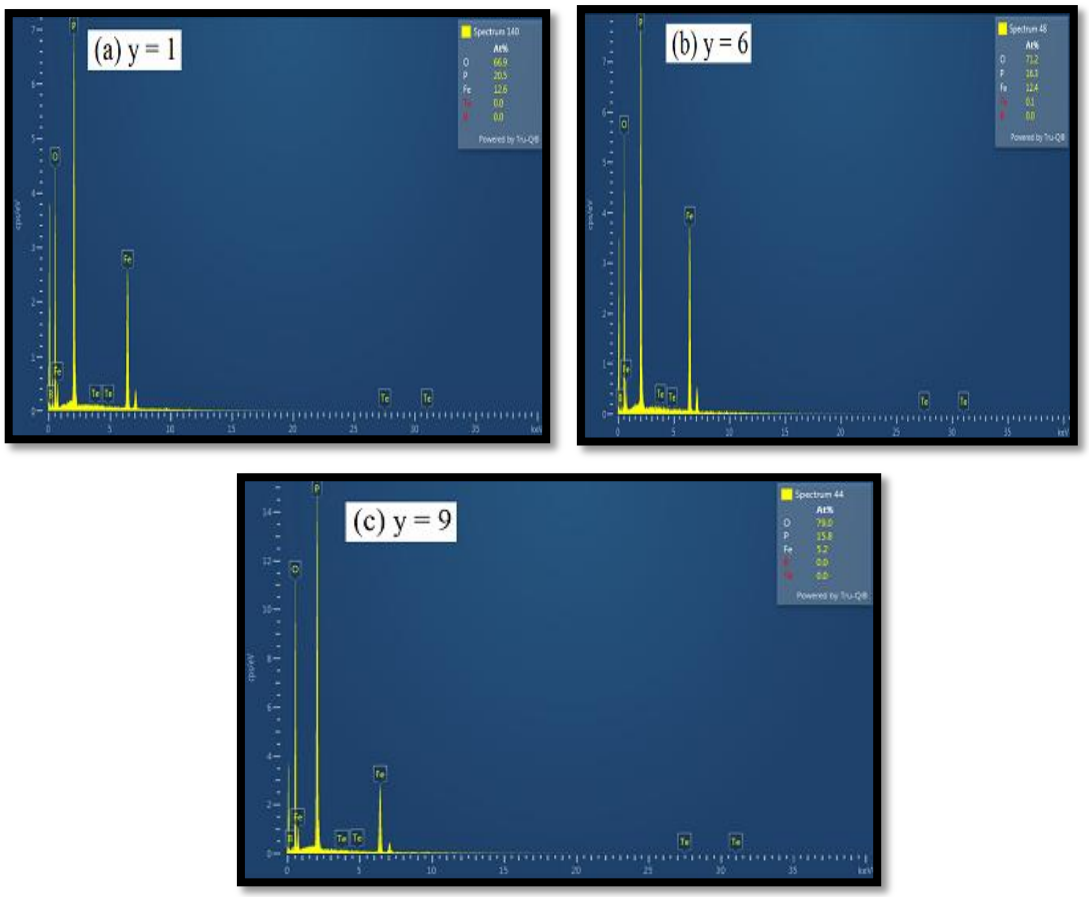


Figure 1.9 EDS Spectrum of $yTeO_2(100-y)[36Fe_2O_3.10B_2O_3.54P_2O_5]$

Table 4 The elements of each sample composition $yTeO_2(100-y)[36Fe_2O_3.10B_2O_3.54P_2O_5]$ nanoparticles analyzed by (Weight %) obtained by EDS

Sr. No	Composition	Elemental Composition (Weight %)				
	y	B	O	P	Fe	Te
1.	1	0.10	49.09	23.15	27.33	0.33
2.	6	0.13	48.43	21.50	29.61	0.36
3.	9	0.15	59.23	25.21	15.06	0.34

Table 5 The elements of each sample composition $yTeO_2(100-y)[36Fe_2O_3.10B_2O_3.54P_2O_5]$ nanoparticles analysed by (Atomic %) obtained by EDS

Sr. No	Composition	Elemental Composition (Atomic %)				
	y	B	O	P	Fe	Te
1.	1	0.03	66.78	20.50	12.60	0.09
2.	6	0.08	71.03	16.30	12.40	0.09
3.	9	0.08	77.23	17.00	5.60	0.09

1.3.6 Raman Study

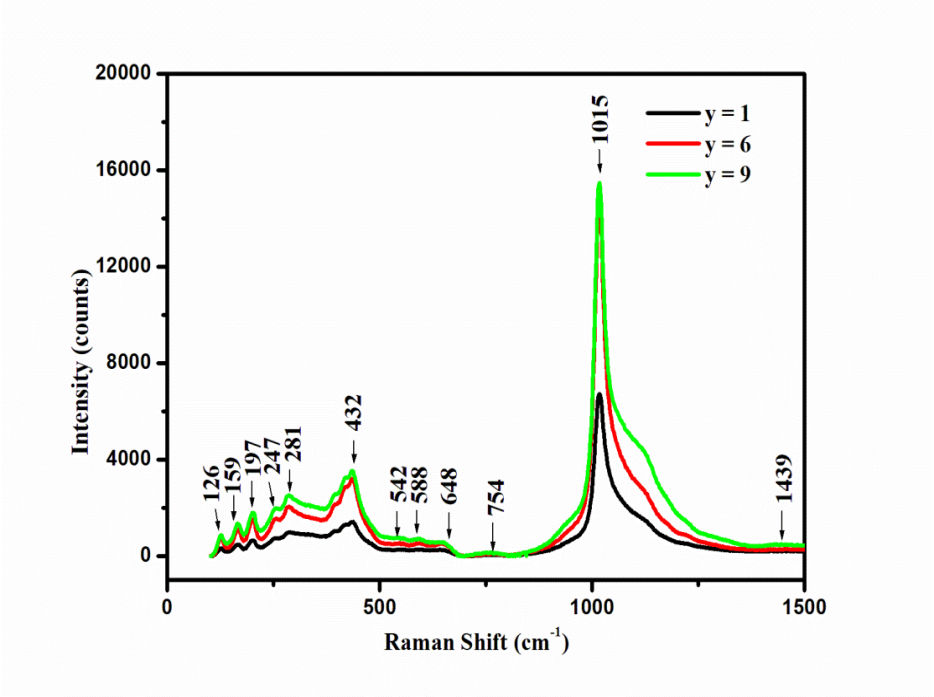


Figure 1.10 Raman Spectra of $yTeO_2(100-y)[36Fe_2O_3.10B_2O_3.54P_2O_5]$

Raman spectra, in the wave number region between 100 to 1500 cm^{-1}, of the synthesised $yTeO_2(100-y)[36Fe_2O_3.10B_2O_3.54P_2O_5]$ glass ceramic material are shown in **Figure 1.10.** For the Tellurium doped iron borophosphate glass ceramic, Raman peaks occur at 126 cm^{-1}, 159 cm^{-1}, 197 cm^{-1}, 247 cm^{-1}, 281 cm^{-1}, 432 cm^{-1}, 542 cm^{-1}, 588 cm^{-1}, 648 cm^{-1}, 754 cm^{-1}, 1015 cm^{-1}, 1439 cm^{-1}. The Raman spectrum observes bands between 100 cm^{-1} and 300 cm^{-1}, which are related to the vibration and rotation of metal cations like Fe^{3+} as given in **Table 6**. The band at 432 cm^{-1} is attributed to the bending mode of O-P-O and the bending vibration of Te-O-Te or O-Te-O linkages and Fe-O-Te bridges [37]. The absorption band between 542 cm^{-1} and 588 cm^{-1} principally corresponds to the bending modes of O-P-O. The band at 648 cm^{-1} is assigned to the stretching vibrations of Fe-O-P bonds. The band at 754 cm^{-1} can be attributed to the bending vibrations of B–O–B bonds in $[BO_4]$ units. The peak at 1015 cm-1 consists of a band due to the symmetric stretching vibration of non-bridging oxygen (O–P–O). The bands located at 1439 cm^{-1} are related to the B-O stretching vibrations in different borate groups [38].

Table 6 Raman bands assignment for the studied glasses

Sr. No	Wave number (cm^{-1})	Assignments
1	100–300 cm^{-1}	Vibration and rotation of metal cations like Fe^{3+}
2	380 and 500cm^{-1}	Attributed to the bending mode of O – P – O and the bending vibration of Te – O – Te or O – Te – O linkages diborate
3	642 and 588cm^{-1}	Corresponds to the bending modes of O – P – O
4	648cm^{-1}	Stretching vibrations of Fe – O – P bonds
5	754 cm^{-1}	Attributed to the bending vibrations of B–O–B bonds in [BO4] units
6	1015	Band forms because of Symmetric outstretching oscillation of non- bridging oxygen (O–P–O)
7	1440 cm^{-1}	B-O stretching vibrations in different borate groups

1.3.7 Dielectric Study (Dielectric Constant and Dielectric loss tangent

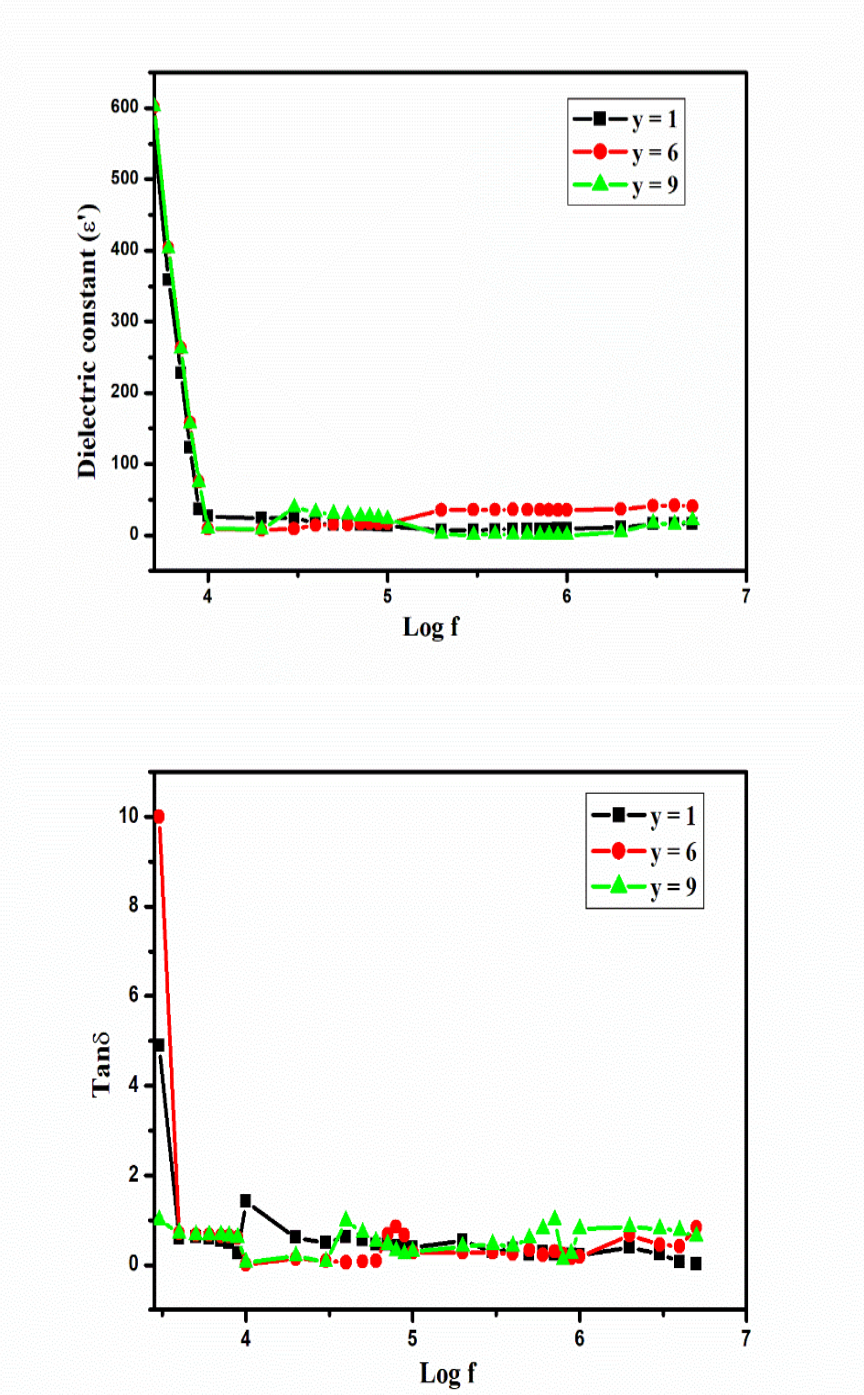


Figure 1.11 (a) variation of dielectric constant with log f (b) variation of dielectric loss tangent (tanδ) with log f for $yTeO_2(100\text{-}y)[36Fe_2O_3.10B_2O_3.54P_2O_5]$series

Figure 1.11(a,b) shows the dielectric constant (ε′) and dielectric loss tangent (tan δ) of a series $yTeO_2(100\text{-}y)[36Fe_2O_3.10B_2O_3.54P_2O_5]$ at different concentrations (y = 1, 6, 9) with frequency ranges from 100 Hz to 20 MHz . Dielectric constant (ε′) has been evaluated from the following relation,

$$\varepsilon' = \frac{Cd}{\varepsilon_0 \pi r^2} \quad \text{---------- (6)}$$

Where C = capacitance, d = thickness, r = radius of the disc-shaped sample, and ε_0 = free space absolute permittivity.

As observed in **Figure 1.11(a)**, the dielectric constant is high at lower frequencies and becomes low at higher frequencies due to looses in their polarization gradually. The high

dielectric value at low frequencies is attributed to the formation of various polarizations, including electronic, ionic, space charge, and orientation polarization. At higher frequencies, the dielectric constant decreases due to the gradual loss of these polarizations. In this range, the applied electric field affects the remaining space charge and orientation polarizations, facilitating electron hopping between various sites within the glass. The incorporation of TeO_2 into the glass network leads to a decrease in the dielectric constant in the glass structure because non-bridging oxygens play a crucial role in the polarization of the glass network [26,39].

The dielectric loss tangent (tan δ) can be evaluated from,

$$(\tan\delta) = \frac{\epsilon''}{\epsilon'} \quad \text{---------- (7)}$$

The dielectric loss tangent has been found to gradually decrease with increasing frequency, as depicted in **Figure 1.11(b).** As a result, Conductivity of the synthesized glass increases significantly with increase in TeO_2 concentration [40].

1.3.8 Antimicrobial activity

$TeO_2(100\text{-}y)[36Fe_2O_3.10B_2O_3.54P_2O_5]$ (y = 1, 6, 9) was found to be antibacterial against Gram positive and Gram negative bacterial and fungal pathogens in all three compounds. However, antimicrobial activity was more against fungi *Aspergillus niger* ATCC 16404 and *Candida albicans* ATCC 10231 as compared to bacteria, indicating its potential use against fungal pathogenic infection. No zone of inhibition was observed with DMSO; the standard drugs Ciprofloxacin and fluconazole showed antibacterial activity against all pathogens in **Table 7.** A minimum inhibitory concentration (MIC) test was performed for all three compounds as per the method and guidelines of the Clinical and Laboratory Standard Institute (CLSI). All experiments were performed in triplicate, and the results were expressed as mean ± SD in µg/mL **Table 8**. The MIC for the selected compounds against *Bacillus Subtilis* ATCC 6633 was found to be 325 ±2.3 µg/mL, 250±1.4 µg/mL, and 650±1.5 µg/mL for the compounds y=1, y=6 and y=9 respectively. MIC for the selected compounds against are *Pseudomonas aeroginosa* ATCC 9027 was 240±1.2 µg/mL, 180±0.8 µg/mL, 200±2.3 µg/mL for the compounds y=1, y=6 and y=9 respectively. The antimicrobial activity against both Gram-positive and Gram-negative pathogens indicates a synergistic effect of these components on microbial growth, which is dependent on their concentrations, as shown in **Figure 1.12.** The Photographic images of Antimicrobial activity of glass material against different microbial pathogens shown in **Figure 1.13.**

Table 7 Antimicrobial activity of glass compounds against microbial Pathogens [a]

Microorganisms	**Y=1**	**Y=6**	**Y=9**	**DMSO**	**Standard[b]**
Bacillus Subtilis ATCC 6633	21	22	17	-	35
Staphylococcus aureus ATCC 6538	12	16	16	-	23
E. coli ATCC 8739	17	15	15	-	16
Pseudomonas aeroginosa ATCC 9027	26	27	25	-	30
Aspergillus niger ATCC 16404	14	14	18	-	23
Candida albicans ATCC 10231	16	17	23	-	27

a- Inhibition zone diameter(mm)

b- Ciprofloxacin and fluconazole was used as antimicrobial standard compound

"-"indicates negative results

Table 8 MIC determination of glass compounds (µg/ml)

Microorganisms	**x=3, Y=2.5**	**x=2, Y=1.5**	**x=1, Y=0.5**	**Standard**
Bacillus Subtilis ATCC 6633	325 ±2.3	250±1.4	650±1.5	35±2.6
Pseudomonas aeroginosa ATCC 9027	240±1.2	180±0.8	200±2.3	30±0.6

In report of tellurium Bio Te BioTe nanoparticles show high antibacterial activity against *Escherichia coli* due to membrane damage, while tellurite toxicity may be linked to sulfur metabolism [41]. Hybrid tellurium-lignin nanoparticles show strong bactericidal effects against antibiotic-resistant bacteria offering potential as an alternative antimicrobial agent without causing harm to human cells [42].

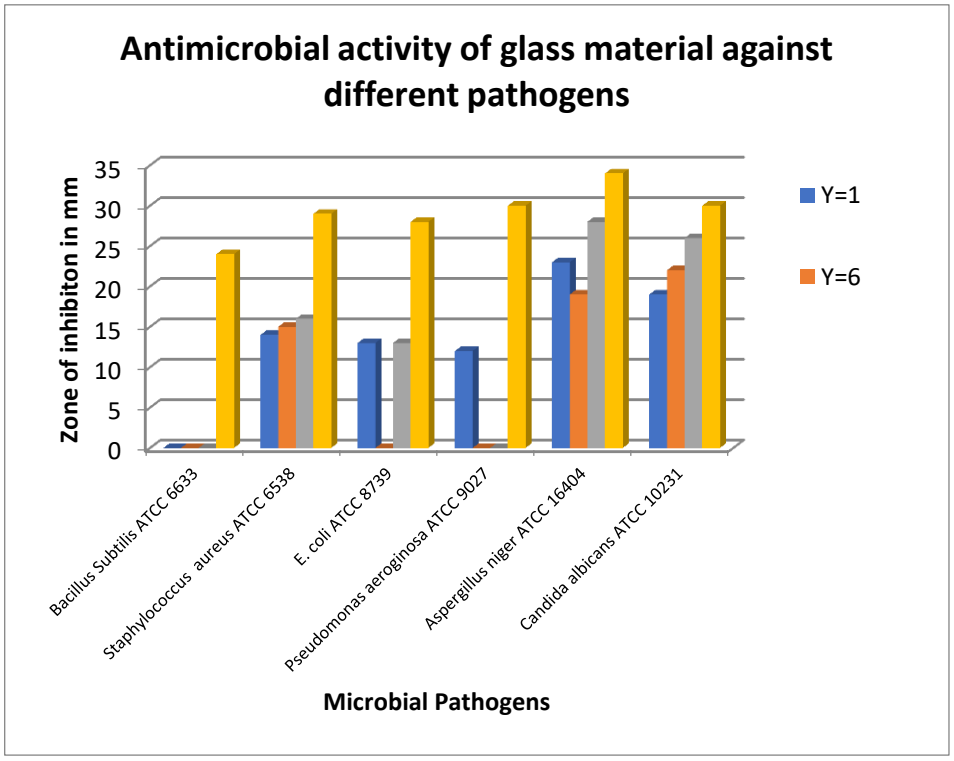
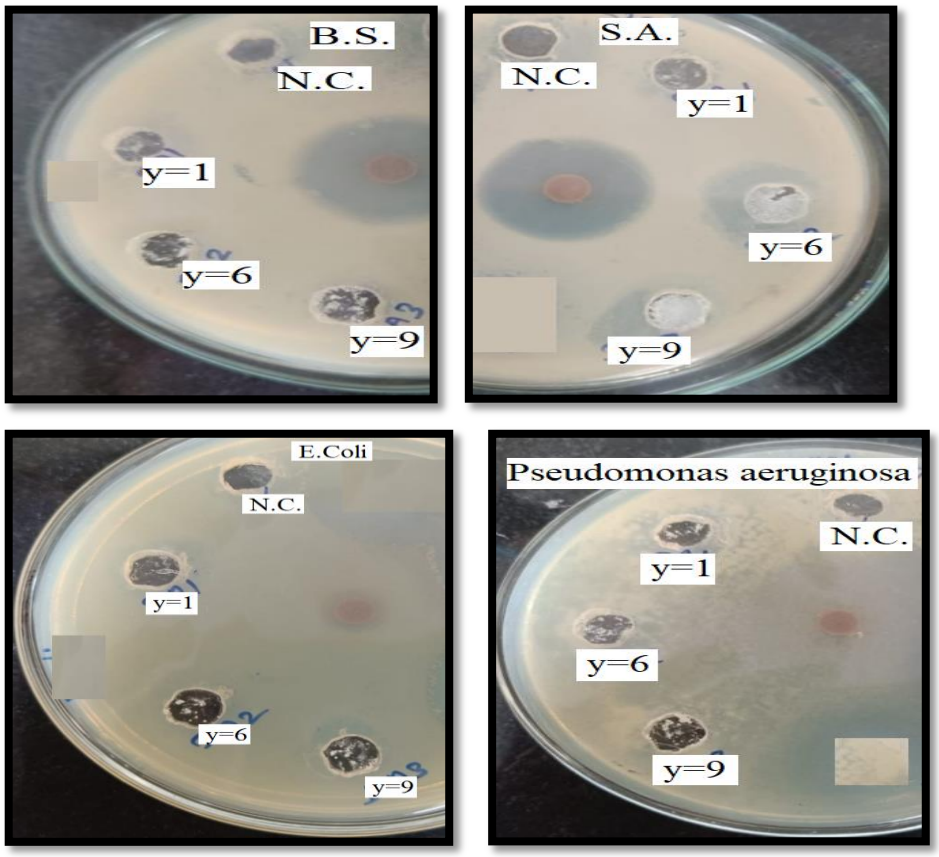


Figure 1.12 Antimicrobial activity of glass material against different microbial pathogens



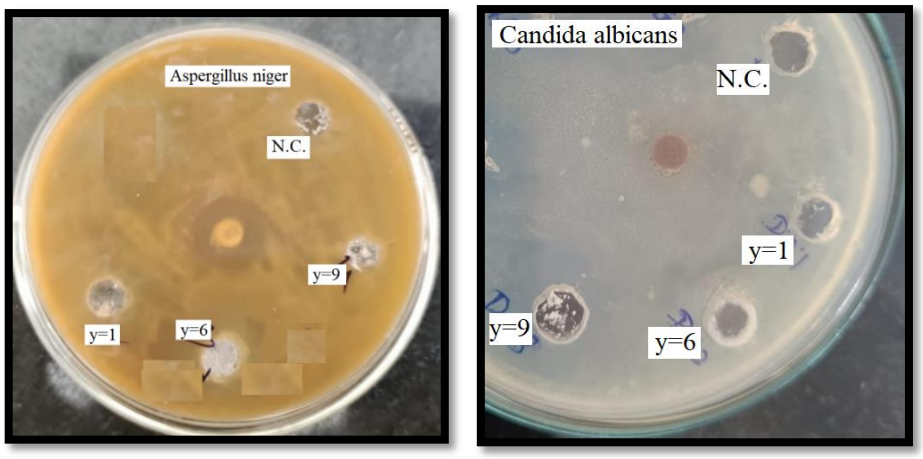


Figure 1.13 Photographic image of Antimicrobial activity of glass material against different microbial pathogens

1.3.9 Anticancer activity

Anticancer activity against human cervical cancer cell lines HeLa showed that increase in drug concentration d results in decrease in the growth of cancerous cell, drug concentration 80 µg/ml results in 50% inhibition of HeLa cell lines. Anticancer activity against human Ovarian cancer cell lines SK-OV-3 showed that increase in drug concentration results in decrease in the growth of cancerous cell, drug concentration 80 µg/ml results in 54.1% inhibition of SK-OV-3 cell lines. Anticancer activity against human Breast cancer cell lines MCF-7 showed that increase in drug concentration results in decrease in the growth of cancerous cell, drug concentration 80 µg/ml results in 46.8% inhibition of MCF-7 cell lines.

Overall this y = 1 compound showed approximately 50% of growth inhibition of the three human cancerous cell lines HeLa, SK-OV-3 and, MCF-7, indicating anticancer properties of this compound. Indicating its anticancer activity. Work by other researcher **also** reported that the tellurium compounds exhibit anticancer properties by inducing oxidative stress, cell cycle arrest, and apoptosis in cancer cells [43-45].

Table 9 Average values for % control growth for the cell line MCF-7

Human Breast Cancer Cell Line MCF-7				
Drug Concentrations (µg/ml)				
	10	**20**	**40**	**80**
Y = 1,6 9	84.9	81.1	72.3	63.4
ADR	-80.4	-80.1	-79.4	-70.0

ADR – Adriamycin, Positive control compound

Table 10 Average values for % control growth for the cell line HeLa

Human Cervical Cancer Cell Line HeLa				
Drug Concentrations (µg/ml)				
	10	**20**	**40**	**80**
y = 1, 6, 9	102.5	100.4	84.0	50.0
ADR	-84.8	-84.5	-81.4	-51.7

ADR – Adriamycin, Positive control compound

Table 11 Average values for % control growth for the cell line SK-OV-3

Human Ovarian Cancer Cell Line SK-OV-3				
Drug Concentrations (µg/ml)				
	10	**20**	**40**	**80**
y = 1, 6, 9	93.1	84.0	76.2	54.1
ADR	-29.2	-53.0	-69.6	-61.9

ADR – Adriamycin, Positive control compound

Table 12 Median growth inhibition (GI50) values for tested compound and ADR

Drug concentrations (µg/ml)		
Cell line	**Name of the drug**	**GI50**
MCF-7	y =1,6,9	>80
	ADR	<10
HeLa	y = 1.6,9	>80
	ADR	<10
SK-OV-3	y = 1,6,9	>80
	ADR	<10

GI50 = Concentration of drug causing 50% inhibition of cell growth

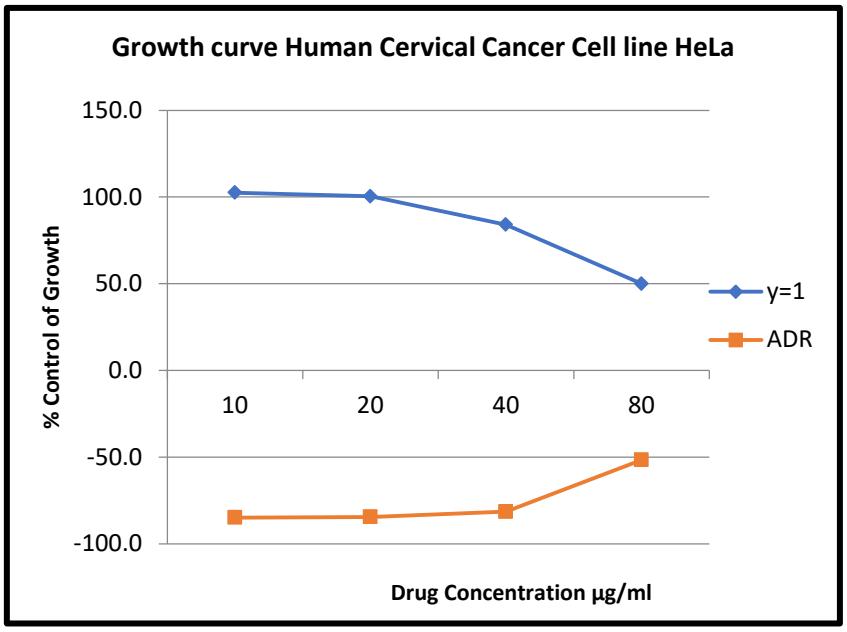


Figure 1.14 Percentage control Growth of Human Cervical Cancer Cell Lines HeLa by (y = 1) and ADR

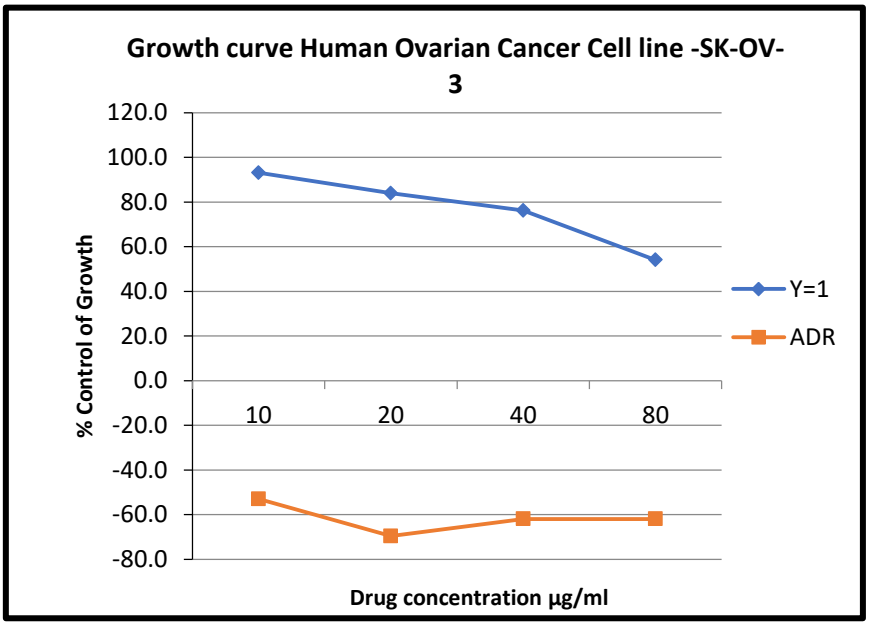


Figure 1.15 Percentage control Growth of Human Ovarian Cancer Cell Lines SK-OV-3 by (y = 1) and ADR

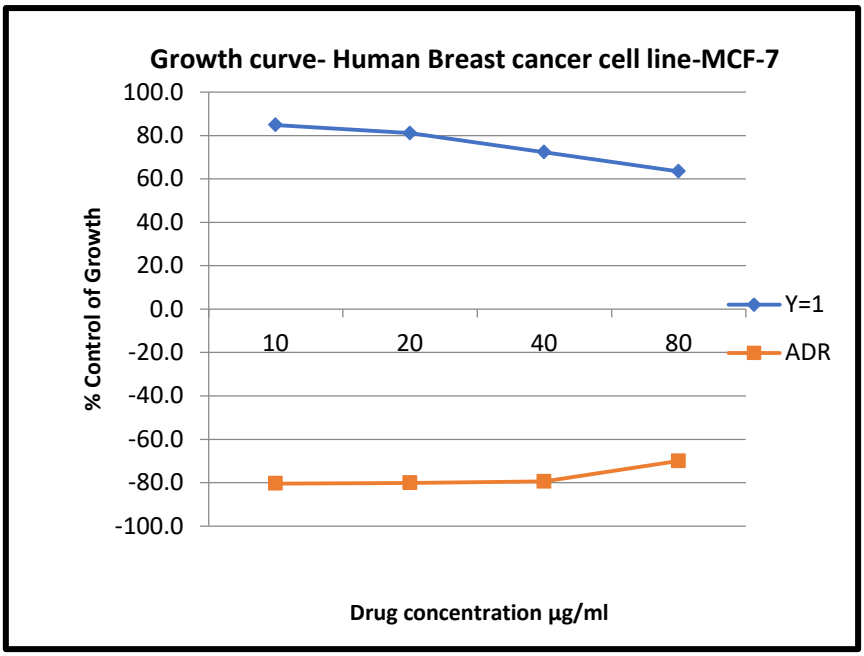
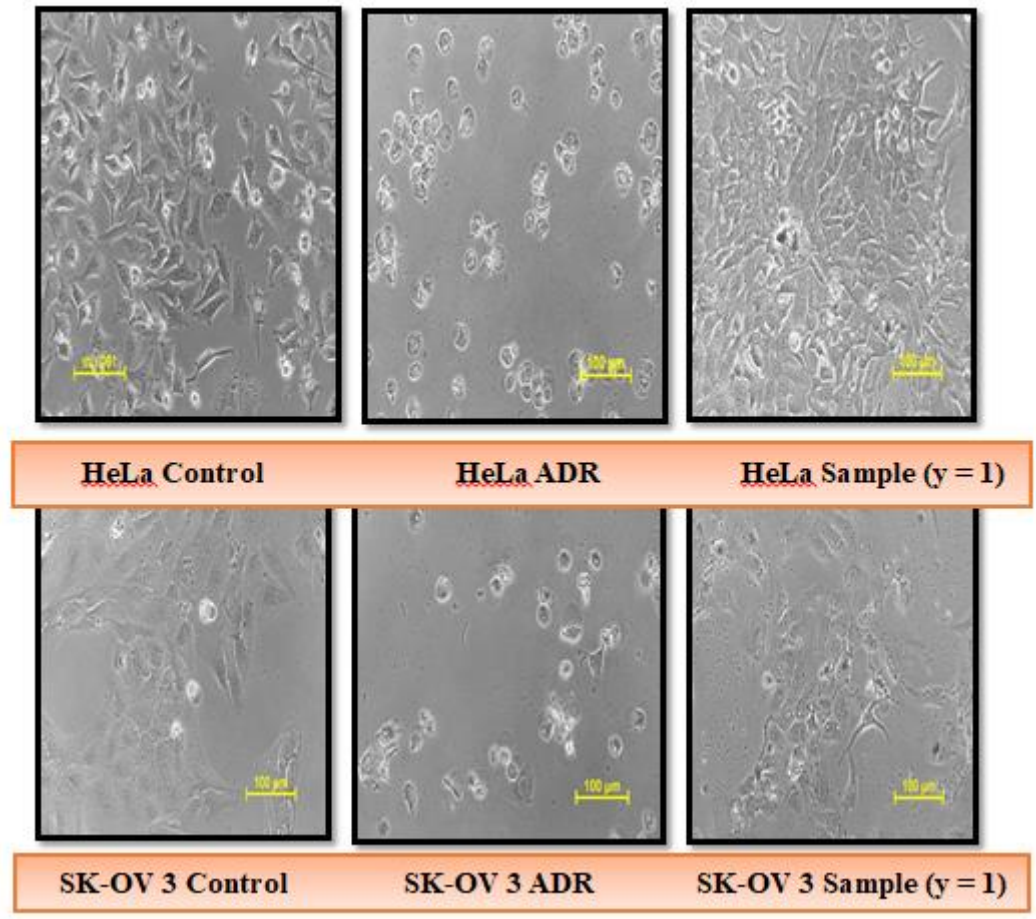


Figure 1.16 Percentage control Growth of Human Breast Cancer Cell Lines MCF-7 by (y =1) and ADR

The images of Anticancer activity of glass material against different cell lines shown in following **figure 4.17**



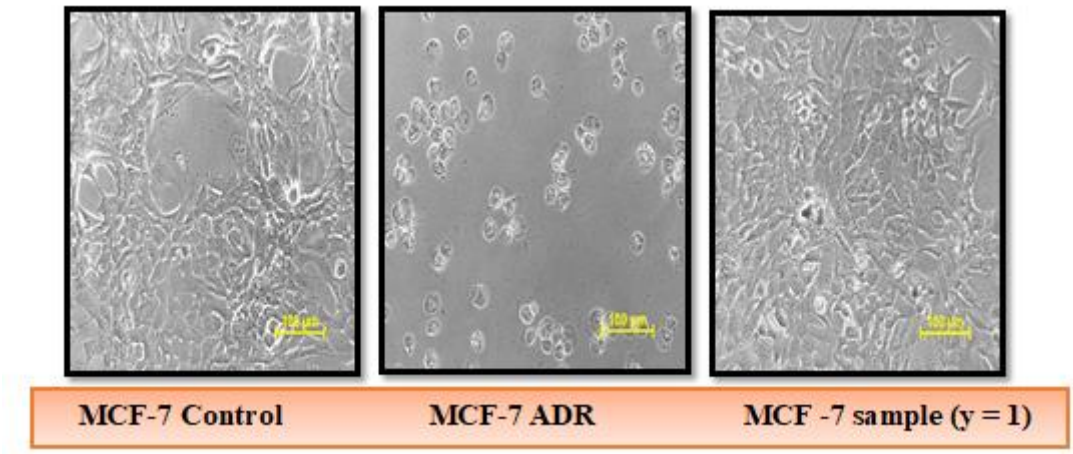


Figure 1.17 The images of Anticancer activity of glass material against different cell lines

1.4 Conclusion

This study reports the iron borophosphate glass material coated by tellurium was successfully synthesized using the sol-gel method. The impact of tellurium oxide on glass series $yTeO_2(100-y)[36Fe_2O_3.10B_2O_3.54P_2O_5]$ at different concentrations (y = 1, 6, 9) was studied by optical, structural, and electrical study. The maximum absorption occurs at 302.07 nm, which has an optical band gap of 4.97 - 4.94 by optical study. In the XRD analysis, The BCC structure was discovered Using the Scherrer formula, and its particle sizes were determined to be in the 9.77-26.68 nm range. According to FE-SEM analysis, glass material shows distinct rounded or courous and porous morphological structure. EDS analysis was used to verify the elemental composition and its purity. According to a Dielectric study, glass can thus be successfully used as a conducting medium because of its low dielectric loss. Based on the findings of investigations on dielectric properties and antimicrobial resistance, the current glass system may be used as a multifunctional material. These glasses have the potential to be used as battery material. Due to its strong biological activity, the glass system can be employed in a variety of medical applications. The antimicrobial activity of our compound was observed against the human pathogens against both Gram positive and Gram negative bacterial and fungal pathogens in all three compounds. *Bacillus Subtilis ATCC 6633*, *Pseudomonas aeroginosa ATCC 9027*, *Aspergillus niger* ATCC 16404 and *Candida albicans* ATCC 10231 showed growth inhibition. The anticancer activity was also reported against human cancerous cell lines HeLa, SK-OV-3 and, MCF-7. Indicating possible use of these compounds as antimicrobial and anticancer agent. Due to its strong biological activity, the glass system can be employed in a variety of medical applications.

Acknowledgment

We are grateful to Dr. Babasaheb Ambedkar Marathwada University Sub–Campus Osmanabad for undertaking this study and to the Dr. Babasaheb Ambedkar Research and Training Institute (BARTI), Pune. Having award letter No. BARTI/Fellowship/BANRF-2018/19-20/3036 for granting to Miss. Vandana Arjun Gaikwad with financial help under the BARTI.

References

1. Bergo P, Reis S, Pontuschka W, Prison JM, Motta C (2004) Dielectric Properties and Structural Features of Barium–Iron Phosphate Glasses. Journal of Non-Crystalline Solids 336. doi: https://doi.org/ 10.1016/j.jnoncrysol.2004.02.008
2. Bergo P, Pontuschka W, Prison JM (2008) Dielectric properties and physical features of phosphate glasses containing iron oxide. Materials Chemistry and Physics 108:142-146. doi: https://doi.org/ 10.1016/j.matchemphys.2007.09.021
3. Joseph K, Govindan Kutty KV, Chandramohan P, Vasudeva Rao PR (2009) Studies on the synthesis and characterization of cesium-containing iron phosphate glasses. Journal of Nuclear Materials 384 (3):262-267. doi:https://doi.org/10.1016/j.jnucmat.2008.11.016

4. Larink D, Eckert H, Reichert M, Martin SW (2012) Mixed Network Former Effect in Ion-Conducting Alkali Borophosphate Glasses: Structure/Property Correlations in the System $[M_2O]_{1/3}[(B_2O_3)_x(P_2O_5)1–x]_{2/3}$ (M = Li, K, Cs). The Journal of Physical Chemistry C 116 (50):26162-26176. doi: https://doi.org/ 10.1021/jp307085t
5. Moguš-Milanković A, Pavić L, Ertap H, Karabulut M (2012) Polaronic Mobility in Boron Doped Iron Phosphate Glasses: Influence of Structural Disorder on Summerfield Scaling. Journal of the American Ceramic Society 95 (6):2007-2014. doi:https://doi.org/10.1111/j.1551-2916.2012.05149.x
6. Sengupta P (2012) A review on immobilization of phosphate containing high level nuclear wastes within glass matrix – Present status and future challenges. Journal of Hazardous Materials 235-236:17-28. doi:https://doi.org/10.1016/j.jhazmat.2012.07.039
7. Srinivasulu K, Omkaram I, Obeid H, Suresh Kumar A, Rao JL (2012) Structural Investigations on Sodium–Lead Borophosphate Glasses Doped with Vanadyl Ions. The Journal of Physical Chemistry A 116 (14):3547-3555. doi: https://doi.org/ 10.1021/jp210398k
8. IBRAHIMa S, MMG, *, HD (2014) Influence of Fe2O3 on the physical, structural and electrical properties of sodium lead borate glasses. Journal of Advanced Ceramics 3 (2):155-164. doi: https://doi.org/ 10.1007/s40145-014-0107-z
9. Stefan R, Karabulut M (2014) Structural properties of iron containing calcium-magnesium borophosphate glasses. Journal of Molecular Structure 1071:45-51. doi:https://doi.org/10.1016/j.molstruc.2014.04.054
10. Karabulut M, Aydın C, Ertap H, Yüksek M (2015) Structure and properties of hafnium iron borophosphate glass-ceramics. Journal of Non-Crystalline Solids 411:19-25. doi:https://doi.org/10.1016/j.jnoncrysol.2014.12.014
11. Dalal S, Khasa S, Dahiya MS, Agarwal A, Yadav A, Seth VP, Dahiya S (2015) Effect of substituting iron on structural, thermal and dielectric properties of lithium borate glasses. Materials Research Bulletin 70:559-566. doi:https://doi.org/10.1016/j.materresbull.2015.05.017
12. Massera J, Shpotyuk Y, Sabatier F, Jouan T, Boussard-Plédel C, Roiland C, Bureau B, Petit L, Boetti NG, Milanese D, Hupa L (2015) Processing and characterization of novel borophosphate glasses and fibers for medical applications. Journal of Non-Crystalline Solids 425:52-60. doi:https://doi.org/10.1016/j.jnoncrysol.2015.05.028
13. Wang F, Liao Q, Dai Y, Zhu H (2015) Properties and vibrational spectra of iron borophosphate glasses/glass-ceramics containing lanthanum. Materials Chemistry and Physics 166:215-222. doi:https://doi.org/10.1016/j.matchemphys.2015.10.005
14. Wang F, Liao Q, Zhu H, Dai Y, Wang H (2016) Crystallization of cerium containing iron borophosphate glasses/glass-ceramics and their spectral properties. Journal of Molecular Structure 1109:226-231. doi:https://doi.org/10.1016/j.molstruc.2016.01.017
15. Zhu H, Liao Q, Wang 王F, Dai Y, Lu M (2016) The effects of chromium oxide on the structure and properties of iron borophosphate glasses. Journal of Non-Crystalline Solids 437:48-52. doi: https://doi.org/ 10.1016/j.jnoncrysol.2016.01.013
16. Sobhanachalam P, Vijaya Kumari C, Sahaya Baskaran G, Syam Prasad P, Veeraiah N, Ravi Kumar V (2017) On identifying efficient modifier oxide in improving bioactivity of Fe2O3 doped calcium oxy fluoro borophosphate glasses. Journal of Alloys and Compounds 692:219-226. doi:https://doi.org/10.1016/j.jallcom.2016.09.037
17. Bae J-H, Cha J-M, Kim D-S, Kim Y-S, Ryu B-K (2018) Structure and Antibacterial Property of ZnO-B_2O_3-P_2O_5 Glasses. J Korean Ceram Soc 55 (2):135-139. doi: https://doi.org/ 10.4191/kcers.2018.55.2.03
18. Ouis M, Fayad A, Abd El Aty A, El-Bassyouni G (2018) Processing, Characterization and Application of Some Borophosphate Glasses Containing Antibacterial and Antifungal Oxides in Bioactive Demands. Egyptian Journal of Chemistry 61. doi: https://doi.org/ 10.21608/ejchem.2018.2229.1184
19. Belusso LCS, Lenz GF, Fiorini EE, Pereira AJ, Sequinel R, Bini RA, Felix JF, Schneider R (2019) Synthesis of silver nanoparticles from bottom up approach on borophosphate glass and their applications as SERS, antibacterial and glass-based catalyst. Applied Surface Science 473:303-312. doi:https://doi.org/10.1016/j.apsusc.2018.12.155

20. ElBatal HA, El-Kheshen AA, Ghoneim NA, Marzouk MA, ElBatal FH, Fayad AM, Abdelghany AM, El-Beih AA (2019) In Vitro Bioactivity Behavior of Some Borophosphate Glasses Containing Dopant of ZnO, CuO or SrO Together with their Glass-Ceramic Derivatives and their Antimicrobial Activity. Silicon 11 (1):197-208. doi: https://doi.org/ 10.1007/s12633-018-9845-9
21. Mošner P, Kupetska O, Koudelka L, Kalenda P (2019) Physical properties and structural studies of lithium borophosphate glasses containing TeO_2. Journal of Solid State Chemistry 270:547-552. doi:https://doi.org/10.1016/j.jssc.2018.12.006
22. Wang Y, Wang F, Wang Q, Zhu H, Xiang G, Liao Q, Zhu Y (2019) Effect of neodymium on the glass formation, dissolution rate and crystallization kinetic of borophosphate glasses containing iron. Journal of Non-Crystalline Solids 526:119726. doi:https://doi.org/10.1016/j.jnoncrysol.2019.119726
23. Haily EM, Bih L, Abdeslam EB, Lahmar A, El Marssi M, Manoun B (2020) Structural, optical, and dielectric properties of the $BaO–TiO_2–P_2O_5$ glasses. Journal of the Australian Ceramic Society. doi: https://doi.org/ 10.1007/s41779-020-00473-1
24. El-Kady AM, Ali AA, El-Fiqi A (2020) Controlled delivery of therapeutic ions and antibiotic drug of novel alginate-agarose matrix incorporating selenium-modified borosilicate glass designed for chronic wound healing. Journal of Non-Crystalline Solids 534:119889. doi:https://doi.org/10.1016/j.jnoncrysol.2020.119889
25. Ibrahim AM (2020) Structural, optical and electrical investigation of sodium phosphate glasses doped MoO_3 for high power visible laser safety. Materials Chemistry and Physics 252:123237. doi:https://doi.org/10.1016/j.matchemphys.2020.123237
26. Naresh P, Padmaja A, Kumar KS (2020) Influence of zinc oxide addition on the biological activity and electrical transport properties of $TeO_2–Li_2O–B_2O_3$ glasses. Materialia 9:100575. doi:https://doi.org/10.1016/j.mtla.2019.100575
27. Abo-Mosallam HA (2021) Influences of SrO on the structure, thermo-physical and chemical properties of zinc iron borophosphate glasses as host matrices for radioactive waste. Journal of Non-Crystalline Solids 571:121084. doi:https://doi.org/10.1016/j.jnoncrysol.2021.121084
28. Palakurthy Srinath PAA, K. Venugopal Reddy (2021) Sol-Gel Synthesis of Soda Lime Silica-Based Bioceramics Using Waste as Renewable Sources. Research square:1-31. doi:https://doi.org/10.21203/rs.3.rs-703473/v1
29. Chen Q, Li Z, Miao B, Ma Q (2021) Thermal, nonlinear, magnetic and faraday rotation properties of sol-gel diamagnetic glass /$NaYF_4$: Fe, Ho^{3+}: Role of magnetic ions. Journal of Alloys and Compounds 858:157631. doi:https://doi.org/10.1016/j.jallcom.2020.157631
30. Lepry WC, Nazhat SN (2021) A Review of Phosphate and Borate Sol–Gel Glasses for Biomedical Applications. Advanced NanoBiomed Research 1 (3):2000055. doi:https://doi.org/10.1002/anbr.202000055
31. da Silva LCA, Neto FG, Pimentel SSC, Palácios RdS, Sato F, Retamiro KM, Fernandes NS, Nakamura CV, Pedrochi F, Steimacher A (2021) The role of Ag_2O on antibacterial and bioactive properties of borate glasses. Journal of Non-Crystalline Solids 554:120611. doi:https://doi.org/10.1016/j.jnoncrysol.2020.120611
32. Miola M, Massera, J., Cochis, A., Kumar, A., Rimondini, L., & Verné, E. (2021). Tellurium: A new active element for innovative multifunctional bioactive glasses.. (2021) Tellurium: A new active element for innovative multifunctional bioactive glasses. Materials science & engineering C, Materials for biological applications 123:111957. doi:https://doi.org/10.1016/j.msec.2021.111957.
33. Medina-Cruz D, Vernet-Crua, A., Mostafavi, E., González, M., Martínez, L., D., A., Kusper, M., Sotelo, E., Gao, M., Geoffrion, L., Shah, V., Guisbiers, G., Cholula-Díaz, J., Guillermier, C., Khanom, F., Huttel, Y., García-Martín, J., & Webster, T. (2021) Aloe Vera-Mediated Te Nanostructures: Highly Potent Antibacterial Agents and Moderated Anticancer Effects. . Nanomaterials 11. doi:https://doi.org/10.3390/nano11020514.
34. Cruz D, Tien-Street, W., Zhang, B., Huang, X., Crua, A., Nieto-Argüello, A., Cholula-Díaz, J., Martínez, L., Huttel, Y., González, M., García-Martín, J., & Webster, T. (2019) Citric Juice-mediated Synthesis of Tellurium Nanoparticles with Antimicrobial and Anticancer Properties.

Green chemistry : an international journal and green chemistry resource : GC, 21 (8):1982-1988 . . doi:https://doi.org/10.1039/C9GC00131J.
35. Abreu H, Lallukka, M., Miola, M., Spriano, S., Verné, E., Raineri, D., Leigheb, M., Ronga, M., Cappellano, G., & Chiocchetti, A. (2024) Human T-Cell Responses to Metallic Ion-Doped Bioactive Glasses. . International Journal of Molecular Sciences 25. doi: https://doi.org/10.3390/ijms25084501
36. Elbatal H, El-Kheshen, A., Ghoneim, N., Marzouk, M., ElBatal, F., Fayad, A., Abdelghany, A., & El-Beih, A. (2019) In Vitro Bioactivity Behavior of Some Borophosphate Glasses Containing Dopant of ZnO, CuO or SrO Together with their Glass-Ceramic Derivatives and their Antimicrobial Activity. Silicon, 11:197-208. . doi:https://doi.org/10.1007/s12633-018-9845-9.
37. Albassam M, Lakshminarayana G, Baki SO, Mohamed Kamari H, Kityk I (2017) Structural, thermal, optical and dielectric studies of Dy^{3+}: B_2O_3 -ZnO-PbO-Na_2O-CaO glasses for white LEDs application. Optical Materials 73. doi: https://doi.org/ 10.1016/j.optmat.2017.09.030
38. Li J, Zhang Y, Nian S, Wu Z, Cao W, Zhou N, Wang D (2017) Glass formation and structure of calcium antimony phosphate glasses and those doped with tellurium oxide. Applied Physics A 123 (3):205. doi: https://doi.org/ 10.1007/s00339-016-0739-7
39. Al-B. F.A. Mohammed GL, S.O. Baki b, M.K. Halimah, I.V. Kityk, M.A. Mahdi (2017) Structural, thermal, optical and dielectric studies of Dy^{3+}: B_2O_3-ZnOPbO-Na_2O-CaO glasses for white LEDs application. Optical Materials 73:686-694. doi:https://doi.org/10.1016/j.optmat.2017.09.030
40. Guntu RK (2019) Luminescence and dielectric properties of Ni^{2+} ions added to calcio yttria borophosphate glasses for optoelectronic uses. Journal of Luminescence 209: 258–266. doi:https://doi.org/10.1016/j.jlumin.2019.01.051
41. Tang A, Ren Q, Wu Y, Wu C, Cheng Y (2022) Investigation into the Antibacterial Mechanism of Biogenic Tellurium Nanoparticles and Precursor Tellurite. International Journal of Molecular Sciences 23:11697. doi: https://doi.org/ 10.3390/ijms231911697
42. Morena A, Bassegoda A, Hoyo J, Tzanov T (2021) Hybrid Tellurium–Lignin Nanoparticles with Enhanced Antibacterial Properties. ACS Applied Materials & Interfaces 13. doi: https://doi.org/ 10.1021/acsami.0c22301
43. Noreen A, Rehman A (2019) Oxidative stress mediated cytotoxicity of tellurite in MDA-MB-231 breast cancer cells. Journal of King Saud University - Science 31. doi: https://doi.org/ 10.1016/j.jksus.2019.03.001
44. Noreen A, Rehman, A., Aftab, S., & Shakoori, A. (2019) Antiproliferative effect of oxidative stress induced by tellurite in breast carcinoma cells. . Journal of Cancer Research and Practice 6:68 - 75. . doi:https://doi.org/10.4103/JCRP.JCRP_5_19
45. Sredni B (2012) Immunomodulating tellurium compounds as anti-cancer agents.. . Seminars in cancer biology 22 (1):60-69. doi:https://doi.org/10.1016/j.semcancer.2011.12.003.